Available online at www.sciencedirect.com

ScienceDirect

Underground Space 27 (2026) 92–111

www.keaipublishing.com/undsp

Research Paper

Seismic response of integrated underground-aboveground structure system and simplified analysis methods for drift ratio and vertical displacement

Jia-Ke Yu [a,b], Jun-Guang Huang [c], Meng-Xiong Tang [d], Jian-Min Zhang [e], Rui Wang [e,*]

[a] *Research Center of Coastal and Urban Geotechnical Engineering, Zhejiang University, Hangzhou 310058, China*
[b] *Zhejiang Huadong Geotechnical Investigation & Design Institute Co., Ltd., Hangzhou 310030, China*
[c] *Guangzhou Design Institute Group Co., Ltd., Guangzhou 510030, China*
[d] *Guangzhou Municipal Construction Group Co., Ltd., Guangzhou 510030, China*
[e] *Department of Hydraulic Engineering, State Key Laboratory of Hydroscience and Engineering, Tsinghua University, Beijing 100084, China*

Received 23 September 2025; received in revised form 26 November 2025; accepted 2 December 2025
Available online 19 January 2026

Abstract

The seismic response of underground structures within integrated underground-aboveground structure system (IUASS) is influenced by both kinematic effect from the surrounding soil and inertia effect from aboveground structures, leading to complex dynamic responses. This paper investigates the seismic response of underground structures in IUASS. Dynamic simulations are conducted using both elastic and elastoplastic constitutive models. The results show that the mean period of input motion and the fundamental period of the free field significantly influence the drift ratio of the underground structure, while the force at the base of the aboveground structure is also strongly correlated with the drift ratio of the underground structure. The vertical displacement of the underground structure is strongly affected by the weight of the IUASS and excess pore pressure generated in the soil. Simplified analysis methods for predicting drift ratio and vertical displacement are subsequently proposed taking these factors into consideration. The proposed methods exhibit excellent agreement with dynamic analysis results across a wide range of input motion and structure conditions, providing important tools for seismic design of IUASS.

Keywords: Integrated underground-aboveground structure system; Seismic response; Dynamic simulation; Period; Simplified analysis method

1 Introduction

With a continuous increase in urban population, major cities around the world are ambitiously developing their underground space (Bélanger, 2007; Ma et al., 2022). Various types of integrated underground-aboveground structure systems (IUASS) have emerged, including residential buildings with underground parking, integrated commercial complexes, and multifunctional transportation hubs (China Ministry of Natural Resources, 2020). Due to the densely populated nature and lifeline function of IUASSs, their seismic safety is a crucial aspect of urban disaster prevention.

It is traditionally considered that the seismic response of underground structures is mainly governed by the surrounding soil (Iida et al., 1996; Iwatate et al., 2000; Bhalla et al., 2005; Hashash et al., 2001; Ramazi & Jigheh, 2006), especially in the liquefiable site (Azadi & Hosseini, 2010; Bao et al., 2017; Chen et al., 2015, 2017). However, for IUASSs, the seismic response of the underground structure is also substantially influenced by the dynamic response of the interconnected aboveground structure (Liu et al., 2022; Scarfone et al., 2020; Stewart et al., 1999; Qiu et al., 2023; Pitilakis et al., 2014;

* Corresponding author.
E-mail address: wangrui_05@mail.tsinghua.edu.cn (R. Wang).
Peer review under the responsibility of Tongji University

https://doi.org/10.1016/j.undsp.2025.12.001

Rashiddel et al., 2024). Consequently, the seismic response of such systems demonstrates greater complexity compared to traditional isolated underground structures. Several studies have indicated that aboveground structures can amplify interconnected underground structure drift ratio, a key parameter for evaluating the deformation of underground structures under earthquake loading (Wang et al., 2022; Zhu et al., 2021a, 2021b). Gillis et al. (2015) and Hashash et al. (2018) investigated the influence of aboveground structures with varying heights on the seismic response of underground structures through centrifuge shaking table tests. The results demonstrated that aboveground structures increase the seismic earth pressure around underground structures, thereby increasing the drift ratio. However, some studies have observed an opposite trend, indicating that aboveground structures may reduce the seismic response of underground structures under certain circumstances (He, 2011). Wang et al. (2018) conducted shaking table tests to investigate the effects of aboveground structures on adjacent tunnel structures under different seismic input motions. They found that aboveground structures reduced the acceleration response of underground structures. Li et al. (2023) conducted numerical simulations to study the influence of high-rise aboveground structures on interconnected large underground structures. They observed that, under specific seismic input motions, the deformation of the aboveground structure could become out of phase with that of the connected underground structure, leading to a reduction in the drift ratio of the underground structure.

Aside from racking deformation, uplift is also one of the common failure modes of underground structures under earthquakes, especially in liquefiable sites. Zhu et al. (2021c) and Rashiddel et al. (2024) employed elastoplastic solid–fluid coupled numerical simulations to study the effect of aboveground structures on the uplift of underground structures in liquefiable sites. Their findings indicate that aboveground structures can significantly suppress the uplift of underground structures. While progress has been made in revealing the influence of aboveground structures on the drift ratio and uplift of underground structures, a comprehensive explanation and quantification of such influence is yet to be achieved.

Simplified analysis methods have been successfully adopted in the seismic design of isolated underground structures in simple ground conditions (Pitilakis & Tsinidis, 2013; Xu et al., 2019, 2023b; MOHURD, 2018). Some researchers have further developed seismic fragility analysis methods for underground structures that take into account various influencing factors to derive more reliable predictions (Cui et al., 2023, 2025; Xu et al., 2023a, 2024, 2025a, 2025b). However, without a comprehensive understanding and quantification of the seismic response mechanism of IUASS, their applicability to such structure systems is unclear. Recently, some researchers have attempted to develop simplified methods to incorporate the influence of aboveground structure on the seismic response of underground structures (Liu et al., 2022). Qiu et al. (2021) proposed to directly apply the peak inertia-induced forces from the aboveground structure to the displacement-based pseudo static method for the underground structure. However, the general applicability of these methods is untested, and they are incapable of assessing the uplift or settlement of underground structures under the influence of aboveground structures.

Considering these research gaps, the current study aims to address the following two fundamental issues via a series of numerical simulations: (1) Under what conditions do aboveground structures aggravate or reduce the seismic response of underground structures? (2) How can simplified analysis methods be formulated to effectively characterize such an interaction between interconnected aboveground and underground structures? Section 2 introduces the simulation procedure, IUASS model, constitutive model, and input motion adopted in this study. Section 3 analyzes the seismic response of the IUASS, including the underground structure drift ratio, forces at the base of the aboveground structure, and vertical displacement of the underground structure. Section 4 proposes simplified analysis methods for the seismic design of underground structures within an IUASS.

2 Numerical simulation setup

2.1 Numerical simulation method

Linear elastic and elastoplastic dynamic analyses are both conducted in this study. In the elastic dynamic analysis, the soil is considered a single-phase material, and the finite element method (FEM) is used. In the elastoplastic analysis, coupling between soil and pore water is considered, with the groundwater table at the ground surface. To facilitate solid–fluid coupled simulations, an explicit finite element method–finite volume method (FEM–FVM) solid–fluid coupled method (Li et al., 2024) is used for the dynamic simulation of saturated soil in the GEOSX platform (Fu et al., 2013). For the single-phase analysis, the same simulation platform is adopted with only FEM.

In the coupled analysis, the solid phase is discretized using FEM. The control equation with explicit solution algorithm is adopted:

$$(\boldsymbol{M} + \boldsymbol{C}\Delta t/2)\boldsymbol{a}^{n+1} = \boldsymbol{F}_{n+1} - \mathbf{C}\boldsymbol{v}^{n+1/2} - \boldsymbol{K}\boldsymbol{u}^{n+1}, \tag{1}$$

$$\boldsymbol{v}^{n+1} = \boldsymbol{v}^{n+1/2} + \boldsymbol{a}^{n+1}\frac{\Delta t}{2}, \tag{2}$$

where Δt is the time step, $\boldsymbol{M}$ is the mass matrix, $\boldsymbol{C}$ is the damping matrix, $\boldsymbol{F}$ is the force vector, and $\boldsymbol{u}$, $\boldsymbol{v}$, and $\boldsymbol{a}$ are the displacement, velocity, and acceleration vectors, respectively.

The fluid solver is discretized using FVM. The forward Euler method is adopted for computational efficiency:

$$m^{n+1} - m^n = \left(\sum_L F_L^n\right)\Delta t, \tag{3}$$

$$\rho_f^{n+1} = \frac{m^{n+1}}{V^{n+1}\varphi^{n+1}}, \tag{4}$$

$$p_{\mathrm{p}}^{n+1} = p^{\mathrm{ref}} + \frac{1}{\beta}\left(1 - \frac{\rho^{\mathrm{ref}}}{\rho_{\mathrm{f}}^{n+1}}\right), \tag{5}$$

where p_{p} is the pore pressure, ρ_{f} is the fluid density, φ is the porosity, m is the fluid mass, F_L is the mass velocity from element L calculated by Darcy's law, V is the element volume, p^{ref} is the reference pore pressure, ρ^{ref} is the reference fluid density, and β is the compressibility coefficient of the fluid.

A fully explicit solid–fluid coupled scheme is adopted (Wang, 2020; Yu et al., 2025), following (1) initialization; (2) update solid displacement in the solid solver and transfer the updated porosity to the fluid solver; (3) update fluid pore pressure in the fluid solver using Eqs. (3)–(5) and transfer the updated pore pressure to the solid solver; (4) update solid acceleration based on the momentum conservation equation using Eq. (1); (5) update the solid velocity using Eq. (2). The accuracy and efficiency of the approach has been thoroughly evaluated in previous studies (Yu et al., 2025).

2.2 IUASS model and simulation campaign

Figure 1 illustrates the IUASS model adopted in this study, which consists of three parts, the underground structure, the aboveground structure, and the soil layers. The underground structure, the top of which is level with the ground surface, comprises a single-story, two-span configuration. The underground structure has a height of 5 m and a width of 6 m per span. The Young's moduli of the central column, slab, wall, and baseplate are 5.74, 28.2, 35.8, and 33.8 GPa. The densities are 400, 2078, 2450, and 2450 kg/m^3, respectively. All structural components are modeled using solid elements, and the choice of modulus, density, and cross-section dimensions in Fig. 1(c) is adopted to achieve flexural stiffness (EI), axial stiffness (EA), and mass equivalent with typical underground structures in engineering practice (Chen et al., 2018).

To investigate the influence of aboveground structure height on seismic response, four aboveground structure configurations with different heights are examined, i.e., 0, 5, 10, and 15 stories. Each story follows an identical layout, comprising a two-span structure with a height of 3 m and a span width of 6 m. The Young's moduli of the middle column, side wall, and slab are 4.36, 17.6, and 17.6 GPa. The densities are 315, 1200, and 1200 kg/m^3, again maintaining equivalent flexural stiffness (EI), axial stiffness (EA), and mass equivalent with typical buildings (see Fig. 2).

The ground model width is set at 84 m to allow for boundary distance to exceed three times the maximum dimension of the underground structure, aiming to limit the boundary effects in accordance with the Standard for Seismic Design of Underground Structures (GB/T 51336—2018) (MOHURD, 2018). The soil profile at the site of an underground structure project in Beijing, China is adopted, with 45 m deep sand consisting of 5 layers. The first 4 soil layers are 10 m thick each, and the 5th soil layer is 5 m thick. The shear wave velocity values for each layer are obtained from in-situ measurements, while the void ratio data are obtained from borehole logs at the same site. The detailed geotechnical parameters are provided in Table 1. For simplicity, the structure and the soil share nodes at the contacts, without considering interface properties, which is effective in existing studies (Zhu et al., 2021; Li et al., 2023; Zhao et al., 2024; Xu et al., 2023b). The groundwater table is near the ground surface due to the existence of a river near the site.

The simulation cases considered in this study are listed in Table 2. Both linear elastic and elastoplastic constitutive models are adopted for soil for each case of different above-

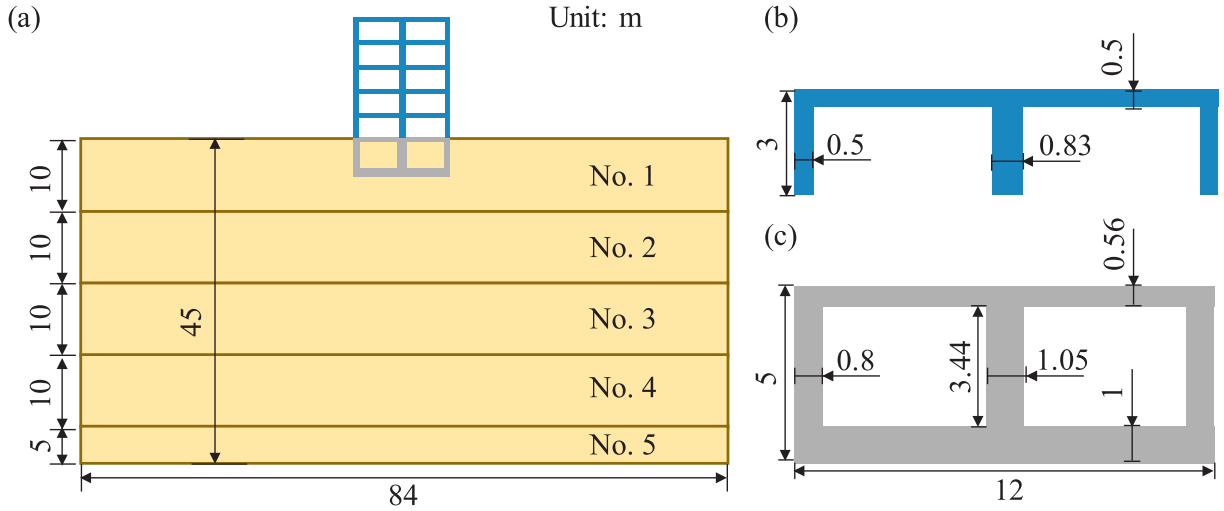

Fig. 1. Numerical model of IUASS. (a) Structure system with aboveground structure, underground structure, and 5 soil layers, (b) one story of the aboveground structure, and (c) underground structure with two spans.

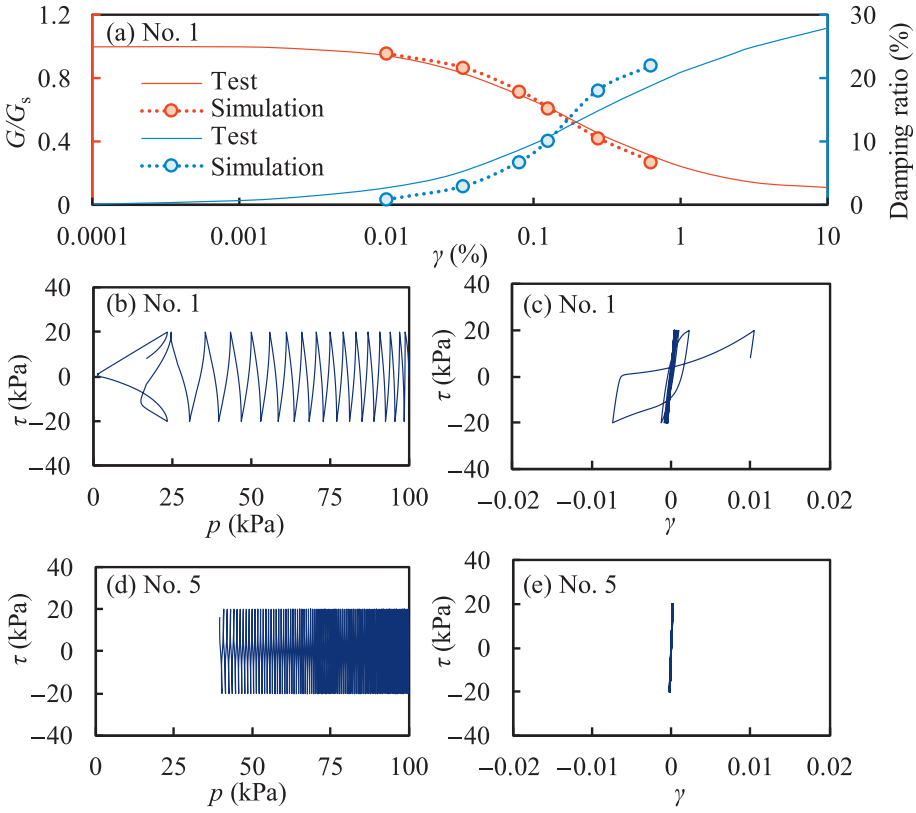

Fig. 2. Shear modulus reduction curve, damping ratio curve, and typical undrained cyclic response simulated using the CycLiq model and calibrated parameters for sand in layers No. 1 and No. 5. (a) Shear modulus reduction curve and damping ratio curve for sand in layer No. 1, (b) shear stress τ versus mean effective pressure p' for sand in layer No. 1, (c) shear stress τ versus shear strain γ for sand in layer No. 1, (d) shear stress τ versus mean effective pressure p' for sand in layer No. 5, and (e) shear stress τ versus shear strain γ for sand in layer No. 5.

Table 1
Soil layer properties.

Case No.	Burial depth (m)	Thickness (m)	Density (kg/m^3)	Shear wave velocity (m/s)	Shear modulus (MPa)	Void ratio
1	10	10	1800	170	52	0.62
2	20	10	1800	250	112	0.62
3	30	10	1900	290	159	0.60
4	40	10	1900	350	232	0.60
5	50	5	2000	500	500	0.57

Table 2
Study cases with different stories.

No.	Aboveground structure stories	Linear elastic simulation	Elastoplastic simulation	Number of input motions
1	0	Yes	Yes	5
2	5	Yes	Yes	5
3	10	Yes	Yes	5
4	15	Yes	Yes	5

ground structure heights to consider both linear elastic and elastoplastic soil conditions. To ensure the generality of the findings, five different input motions are adopted for each case, resulting in a total of 40 simulations. Detailed specifications regarding the constitutive models and input motions are provided in subsequent sections.

2.3 Soil constitutive models

Two constitutive models are adopted in this study. First, a simple linear elastic model is adopted to simulate the soil, aiming to exclude the influence of nonlinearity and plasticity and focus on the role of input motion and IUASS system

period in the influence of aboveground structure on the drift ratio of the connected underground structure. The basic findings from linear elastic analysis are then validated in a more realistic elastoplastic solid–fluid coupled analysis, which also allows for the evaluation of settlement and uplift. For the linear elastic model, the shear modulus values are given in Table 1, with a Poisson's ratio of 0.3. For the elastoplastic model, the CycLiq model is adopted, which was proposed by Wang et al. (2014) and implemented in OpenSEES (Zhu et al., 2021b; He et al., 2020), FLAC3D (Hu-Yan et al., 2024; Wang et al., 2023), and GEOSX (Fu et al., 2013; Wang, 2020). The model has been thoroughly validated and widely applied in the seismic analysis of underground structures (Li et al., 2025; Zhang & Wang, 2024).

The stress–strain response relationship of the CycLiq model can be described by the following equation:

$$\dot{\varepsilon} = \frac{p\dot{\boldsymbol{r}}}{2G} + \left(\frac{\boldsymbol{r}}{2G} + \frac{\boldsymbol{I}}{3K}\right)\dot{p} + \left(\boldsymbol{n} + \frac{D_{\mathrm{re}} + D_{\mathrm{ir}}}{3}\boldsymbol{I}\right)\langle L\rangle, \tag{6}$$

where p is the effective mean stress; $\boldsymbol{r}$ is the ratio of the deviatoric stress tensor $\boldsymbol{s}$ to the stress p; G and K are the elastic shear modulus and bulk modulus; $\boldsymbol{I}$ is the unit tensor; $\boldsymbol{n}$ represents the flow direction and loading direction of plastic deviatoric strain; D_{re} is the reversible dilatancy; D_{ir} is the irreversible dilatancy; L is the plastic loading index. The dot above a variable denotes the rate of the variable.

For the elastic and plastic modulus, the CycLiq model adopts the following equations:

$$G = G_0 \frac{(2.973 - e_{\mathrm{in}})^2}{1 + e_{\mathrm{in}}} p_{\mathrm{a}} \left(\frac{p}{p_{\mathrm{a}}}\right)^{1/2}, \tag{7}$$

$$K = \frac{1 + e_{\mathrm{in}}}{\kappa} p_{\mathrm{a}} \left(\frac{p}{p_{\mathrm{a}}}\right)^{1/2}, \tag{8}$$

$$H = \frac{2}{3} hG \exp\left(-n^{\mathrm{p}}\Psi\right) \left[\frac{M \exp\left(-n^{\mathrm{p}}\Psi\right)}{M_{\mathrm{m}}} \left(\frac{\bar{\rho}}{\rho}\right) - 1\right], \tag{9}$$

where e_{in} is the initial void ratio, p_{a} is the atmospheric pressure, ρ is the distance between stress ratio $\boldsymbol{r}$ and back stress ratio $\boldsymbol{\alpha}_{\mathrm{in}}$, $\bar{\rho}$ is the distance between $\bar{\boldsymbol{r}}$ and back stress ratio $\boldsymbol{\alpha}_{\mathrm{in}}$, M_{m} is the maximum stress ratio, G_0, κ, n^{p}, M, and h are the model parameters. Ψ is the state parameter proposed by Been and Jefferies (1985) as $\Psi = e - e_{\mathrm{c}}$, where e is the void ratio and e_{c} is the critical void ratio. The critical void ratio e_{c} can be calculated as $e_{\mathrm{c}} = e_0 - \lambda_{\mathrm{c}}(p/p_{\mathrm{a}})^{\xi}$, where e_0, λ_{c}, and ξ are model parameters.

For dilatancy, the reversible dilatancy D_{re} and irreversible D_{ir} are formulated as

$$D_{\mathrm{re}} = \begin{cases} \sqrt{2/3} d_{\mathrm{re},1}(\boldsymbol{r}_{\mathrm{d}} - \boldsymbol{r}) : \boldsymbol{n}, \ (\boldsymbol{r}_{\mathrm{d}} - \boldsymbol{r}) : \boldsymbol{n} < 0 \\ (d_{\mathrm{re},2}\chi)^2 / p, \ (\boldsymbol{r}_{\mathrm{d}} - \boldsymbol{r}) : \boldsymbol{n} > 0 \end{cases}, \tag{10}$$

$$D_{\mathrm{ir}} = d_{\mathrm{ir}} \exp\left(n^{\mathrm{d}}\Psi - \alpha\varepsilon_{\mathrm{vd,ir}}\right) \left[\begin{array}{l} \langle M \exp\left(n^{\mathrm{d}}\Psi\right) - \eta\rangle \exp\left(\chi\right) \\ + \left(1 + \frac{\gamma_{\mathrm{mono}}}{\gamma_{\mathrm{d,r}}\left\langle 1 - \exp\left(n^{\mathrm{d}}\Psi\right)\right\rangle}\right)^{-2} \end{array}\right], \tag{11}$$

where $d_{\mathrm{re},1}$, $d_{\mathrm{re},2}$, d_{ir}, n^{d}, α, and $\gamma_{\mathrm{d,r}}$ are model parameters. Detailed explanations for the reasoning of the formulation can be found in Wang et al. (2014).

To ensure the initial shear modulus of elastoplastic dynamics is consistent with that of elastic analysis, the elastic parameters (G_0 and κ) are calibrated based on the provided shear modulus listed in Table 1. The other CycLiq parameters are mostly adopted based on the well-calibrated parameters of Ottawa sand (He et al., 2020; Hu-Yan et al., 2024; Wang et al., 2023), with slight alterations to match the shear modulus reduction and damping ratio data available for the soil at the site, which are shown in Table 3. The permeability coefficient of the sand layers is taken as 1.25×10^{-5} m/s.

The shear modulus reduction G/G_{s} curve, damping ratio curve, and typical undrained cyclic response simulated using the CycLiq model and calibrated parameters are illustrated in Fig. 2 for sand in layers No. 1 and No. 5. The shear modulus reduction G/G_{s} curve and damping ratio curve in Fig. 2(a) show good agreement with laboratory test data obtained for the soil at the site. Undrained cyclic shear response is simulated at a cyclic stress ratio (CSR) of 0.2 and an initial confining pressure of 100 kPa. The sand in layer No. 1 with shallower depth is more prone to liquefaction and large deformation than the sand in layer No. 5 with greater depth.

2.4 Input motion

Five seismic input motions with varying frequency characteristics are selected. The acceleration time histories and corresponding power spectrum for all input motions are presented in Fig. 3. These seismic records consist of actual ground motion data, which undergo baseline correction and 10 Hz low-pass filtering, with peak ground acceleration (PGA) scaled to 0.2g. To facilitate subsequent analysis, the seismic input motions (denoted as G1 through G5) are ordered according to their mean periods in ascending

Table 3
Parameters of sand using the CycLiq model.

Sand layer No.	1	2	3	4	5
G_0	170	270	280	350	525
κ	0.012	0.008	0.008	0.006	0.004
h	1.5	1.5	1.5	1.5	1.5
M	1.1	1.1	1.1	1.1	1.1
$d_{\mathrm{re},1}$	1.4	1.4	1.4	1.4	1.4
$d_{\mathrm{re},2}$	30	30	30	30	30
$\gamma_{\mathrm{d,r}}$	0.05	0.05	0.05	0.05	0.05
α	30	30	30	30	30
d_{ir}	2.6	2.6	2.6	2.6	2.6
λ_{c}	0.0112	0.0112	0.0112	0.0112	0.0112
ξ	0.715	0.715	0.715	0.715	0.715
e_0	0.78	0.78	0.78	0.78	0.78
n^{p}	3.2	3	3	2.6	2.6
n^{d}	6	6	6	6	6

order, with G1 exhibiting the shortest mean period (0.40 s) and G5 the longest (0.64 s). The mean period has been reported to be the best simplified frequency content characterization parameter for earthquake ground motion, and is calculated as follows (Rathje et al., 1998):

$$T_{\mathrm{m}} = \frac{\sum_i C_i^2 \frac{1}{f_i}}{\sum_i C_i^2} \quad 0.25\ \mathrm{Hz} \le f_i \le 20\ \mathrm{Hz}, \tag{12}$$

where C_i is the Fourier amplitudes of the input motion, which is shown in the subfigures Fig. 3(a)–(e), and f_i is the discrete Fourier transform frequencies between 0.25 and 20 Hz. The cumulative absolute velocity (CAV) of each input motion is also labelled in the subfigures. The G3 has the largest CAV, while G1 has the smallest CAV. Seismic excitation of the numerical model is applied as horizontal input motions at the base boundaries in both lateral directions.

3 Influence of aboveground structure on underground structure response

3.1 Fundamental period of IUASS

To help understand the role of the aboveground structure, the fundamental period of the IUASS is first determined. In the modal analysis, the bottom boundary of the site is fully fixed, while the lateral boundaries permit only horizontal displacement. Only the initial state of the soil is considered here using the linear elastic parameters in Table 1.

Figure 4 shows the first vibration modes and fundamental periods for the free field T_{f}, the aboveground structures T_1, and the structure–soil system T_{total}. As the height of aboveground structure increases, the fundamental periods of both the aboveground structures and the structure–soil system increase. The aboveground structure fundamental period is always smaller than the corresponding structure–soil system fundamental period, as soil–structure interaction reduces the constraint at the base of the structure. For cases with low aboveground structure (small fundamental period) or no aboveground structure, the fundamental period is mainly governed by the soil, as shown in Fig. 4(b)–(c). For cases with relatively high aboveground structure, the fundamental period of the system is strongly influenced by the aboveground structure, as shown in Fig. 4(e). The terms 'low' and 'high' for aboveground structures are defined based on their influence on the fundamental period of the IUASS in this study. If the aboveground increases the system period by 20%, it can be called the high aboveground. Otherwise, it is called the low aboveground. Under this definition, the 5-story

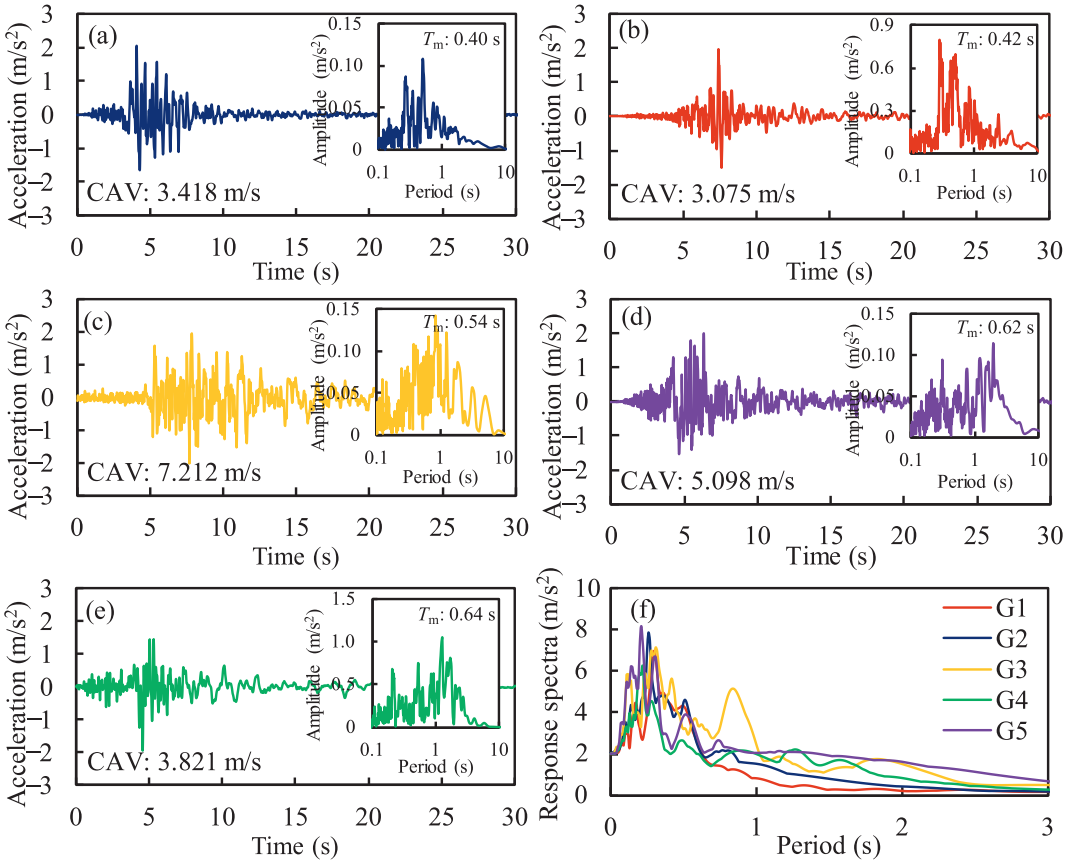

Fig. 3. Seismic input motions in the simulations and their Fourier amplitude and response spectra: (a) G1 Friuli, (b) G2 Park Field, (c) G3San Fernando, (d) G4 Loma Prieta, (e) G5 Livermore, and (f) response spectra (5% damping) of the 5 input motions.

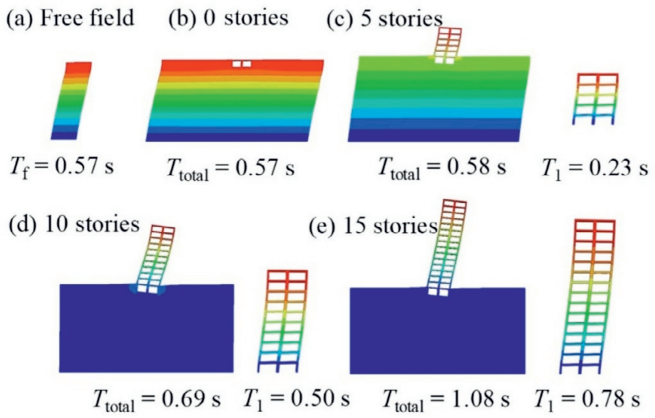

Fig. 4. First vibration mode of the free field, IUASS-soil and aboveground structures, with the fundamental period of free field T_f, IUASS-soil T_{total}, and aboveground structure T_1.

aboveground is low, while the 10- and 15-story aboveground is high.

Figure 5 shows the comparison of the fundamental period of the 4 cases and the mean period of 5 seismic input motions. The mean periods of G1–G3 are less than the fundamental period of all cases, while the mean periods of G4 and G5 are larger than the fundamental periods of free field and IUASS-soil systems with 0 and 5-story aboveground structures. The mean periods of G1–G5 are smaller than the fundamental periods of IUASS-soil with 10- and 15-story aboveground.

3.2 Drift ratio

The influence of input ground motion and aboveground structure height on the drift ratio of underground structures is analyzed in this section. The drift ratio refers to the maximum lateral displacement difference between the top and base of the middle column divided by its height in underground structure during the earthquake. Figure 6 presents the drift ratios of underground structures subjected to 5 input motions, revealing that the variation pattern of drift ratios does not exhibit consistent correlation with the increasing height of aboveground structures. For

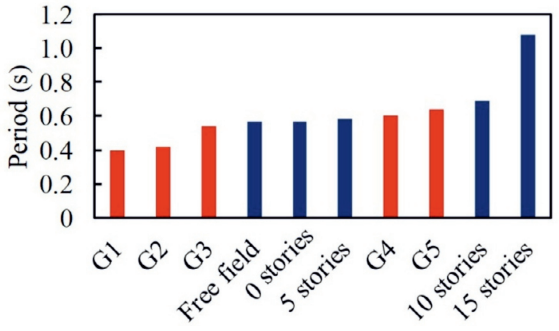

Fig. 5. Comparison of the fundamental period of IUASS-soil system and the mean period of the input motion.

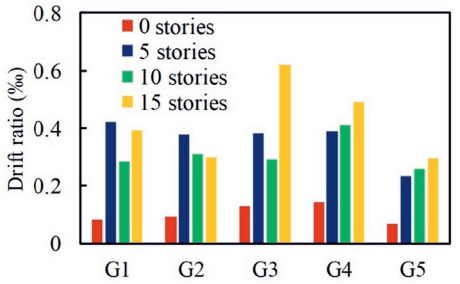

Fig. 6. Drift ratio of underground structure under different input motions.

G4 and G5, where the mean periods of input motions are larger than the system fundamental period, the drift ratios demonstrate a consistent increasing trend with increasing aboveground structure height. However, for G1–G3 with a mean period smaller than the system fundamental period, no consistent relationship between drift ratios and the number of aboveground stories is observed.

When examining the influence of CAV, it can be observed that for ground motions with mean periods longer than the fundamental period of the free field (G4 and G5), a greater CAV (G4 > G5) corresponds to a larger drift ratio, which is consistent with findings from existing studies (Karmer & Mitchell, 2006). However, for ground motions with periods shorter than the fundamental period of the free field (G1, G2, and G3), there is no significant correlation between CAV and drift ratio.

Figure 7 presents a detailed analysis of the drift ratio distribution for a 15-story aboveground structure under input motions G2 and G4, at the moment of maximum drift ratio of the underground structure. The comparison reveals distinct dynamic behaviors: for G2, where the mean period is shorter than the system fundamental period, opposite racking motions are observed between underground and aboveground structures. In contrast, for G4 with a mean period greater than the system fundamental period, underground and aboveground structures drift in synchronous directions. These observations suggest: (1) under short mean period input motions, high aboveground structure racks out of phase with the underground structure and may cause a reduction in the underground structural drift ratio, while (2) under long mean period input motions, high aboveground structure racks in-phase with the underground structure to amplify the drift ratio. This also explains the observations of Li et al. (2023), where numerical simulations similarly identified a reduction in underground structure drift ratio influenced by aboveground structures under short mean period input motions. The results demonstrate that the influence of aboveground structure on the seismic response of underground structure is strongly affected by complex period-dependent interactions.

For elastoplastic dynamic analysis, Fig. 8(a) shows the drift ratio of the 4 cases under different input motions. The drift ratio variation with the height of the aboveground structure is generally consistent with that in

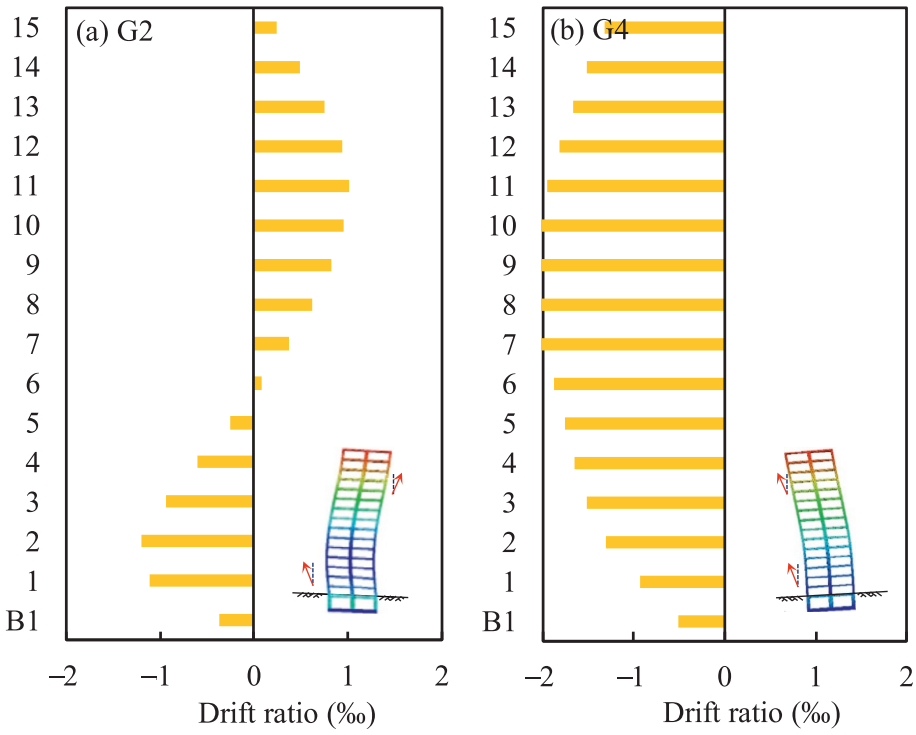

Fig. 7. Drift ratio of 15-story aboveground structure and underground structure at the moment of maximum drift ratio of underground structure in the linear elastic simulations: (a) G2, and (b) G4.

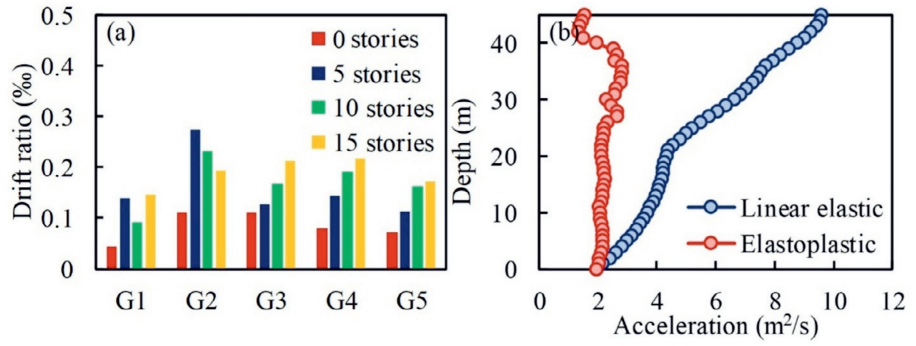

Fig. 8. Drift ratio of underground structure in elastoplastic simulations and comparison of horizontal acceleration between the elastic and elastoplastic simulations. (a) Drift ratio of underground structure under different input motions in elastoplastic simulations, and (b) maximum acceleration at different depths in the free field under G3 in the elastic and elastoplastic simulations.

the linear elastic analysis. The difference is that the drift ratio of the elastoplastic simulation in Fig. 8(a) is generally smaller than that in Fig. 6. This is mainly due to the different accelerations at the surface of the site. Figure 8(b) shows the acceleration distribution in the free field under G3. Under the same input motion at the bottom, the acceleration in the linear elastic simulation is significantly amplified, while the acceleration in the elastoplastic simulation is attenuated due to the nonlinearity and softening of the soil.

These results indicate that when the mean period of input motion is higher or lower than the fundamental period of the structure–soil system, the dependence of underground structure drift ratio on aboveground structure height shows different patterns. Therefore, the relationship between input motion period and system fundamental period is a key factor governing the influence of aboveground structure on interconnected underground structure racking.

To further quantify the influence of aboveground structure on the seismic response of underground structure, the relationship between the force at the base of the aboveground structure and the racking of the underground structure is assessed. This force refers to the axial force, bending moment, and shear force at the base of the middle column. As solid elements are used for the structure, this force is calculated from the stress of each element. Specifically, the 0.83-m-wide middle column is discretized into 4 elements, and the force is then calculated by integrating the

vertical stress and horizontal shear stress from each element over their respective widths. Figure 9 shows the correlation among the maximum axial force, bending moment, and shear force at the base of the aboveground structure and the drift ratio of the underground structure for the linear elastic simulations. The horizontal axis represents the increment ratio of the drift ratio of the underground structure, while the vertical axis represents the increment ratio of axial force, bending moment, and shear force at the base of the aboveground structure. The definition of increment ratio is as follows:

$$r = \frac{\alpha_i - \alpha_5}{\alpha_5}, \tag{13}$$

where r is the increment ratio, α_i can represent the drift ratio or forces (axial force, bending moment, and shear force) for the i-story aboveground structure, and α_5 is the drift ratio or forces for the 5-story aboveground structure. For the case without aboveground structure, the internal forces of the aboveground structure are all 0, and the increment ratio of the internal forces is −1. For the 5-story aboveground structure, all increment ratios are 0. By using Eq. (12), it is possible to eliminate the influence of soil response under different input motions, and only analyze the influence of forces imposed by the aboveground structures.

In the linear elastic simulations, the increment ratios of dynamic forces and drift ratios in Fig. 9 show good correlation. Pearson's correlation coefficients ρ between axial force, bending moment, shear force, and drift ratio are 0.92, 0.86, and 0.91, respectively. All Pearson's correlation coefficients exceed 0.8. Figure 9 also performs linear fitting on the relationship between three forces and drift ratio, with slopes greater than 1.0 and R^2 greater than 0.74. This indicates a strong linear correlation between the drift ratio of underground structures and the dynamic forces imposed by aboveground structures.

For elastoplastic simulations, Fig. 10 shows a similar relationship between the increment ratio of the drift ratio and the increment ratio of forces imposed by the aboveground structure. Pearson's correlation coefficients ρ between axial force, bending moment, shear force, and drift ratio are 0.78, 0.71, and 0.84, respectively. This indicates that the linear correlation applicable to the linear elastic simulations also applies to the elastoplastic simulations.

The results demonstrate that although it is difficult to establish a directional relationship between the aboveground structure height and its influence on the drift ratio of underground structures, the forces imposed by the aboveground structure on the underground structure exhibit simple linear correlation with its influence on the underground structure's drift ratio. Therefore, the forces at the base of the aboveground structure can be a good potential indicator for the influence of the aboveground structure on the seismic response of interconnected underground structure.

It should be noted that the maximum drift ratio of the underground structure and the maximum force at the base of the aboveground structure might not occur simultaneously. Figure 11 presents the time history of the dynamic shear force at the base of the 5-story and 10-story aboveground structures and the drift ratio of the corresponding underground structure under G2 and G4. When it is a 5-story aboveground structure, the dynamic shear and the drift ratio are largely synchronized. However, when it is a 10-story aboveground structure, the shear force is out of phase with the drift ratio. This trend is observed for all five input motions. Therefore, when the aboveground structure height and subsequently fundamental period are relatively large, there is a phase difference between the forces imposed by the aboveground structure and the racking of the underground structure, resulting in complex interaction between the aboveground and underground structures.

3.3 Uplift and settlement

Post-earthquake uplift and settlement of the underground structure can be analyzed in the solid–fluid coupled elastoplastic simulations, which cannot be reflected in the linear elastic simulations. Figure 12(a) shows the uplift

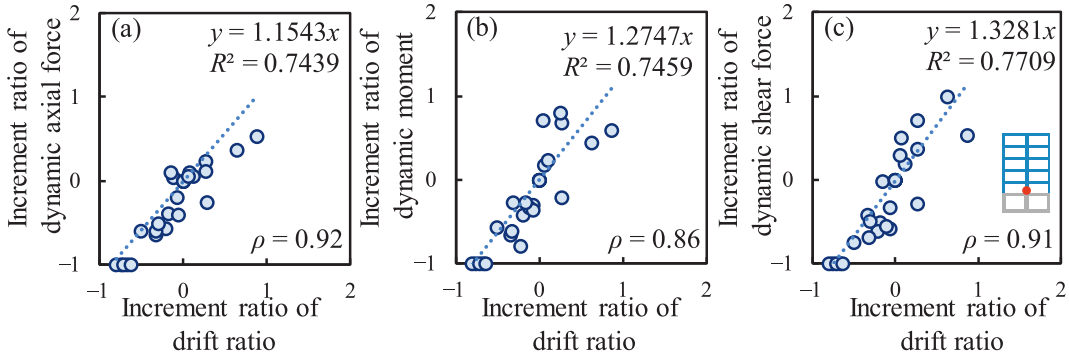

Fig. 9. Relationship between the increment ratio of drift ratio and the increment ratio of dynamic forces at the base of the aboveground structures under different input motions in the linear elastic simulations. (a) Increment ratio of dynamic axial force versus increment ratio of drift ratio with R^2 and Pearson's correlation coefficient ρ, (b) increment ratio of dynamic moment versus increment ratio of drift ratio with R^2 and Pearson's correlation coefficient ρ, and (c) increment ratio of dynamic shear versus increment ratio of drift ratio with R^2 and Pearson's correlation coefficient ρ.

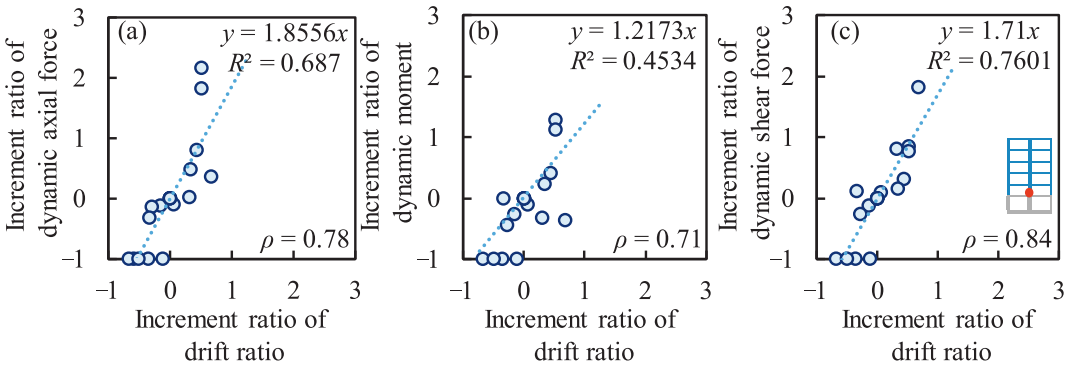

Fig. 10. Relationship between the increment ratio of drift ratio and the increment ratio of dynamic forces at the bottom of the aboveground structures under different input motions in elastoplastic simulations. (a) Increment ratio of dynamic axial force versus increment ratio of drift ratio with R^2 and Pearson's correlation coefficient ρ, (b) increment ratio of dynamic moment versus increment ratio of drift ratio with R^2 and Pearson's correlation coefficient ρ, and (c) increment ratio of dynamic shear versus increment ratio of drift ratio with R^2 and Pearson's correlation coefficient ρ.

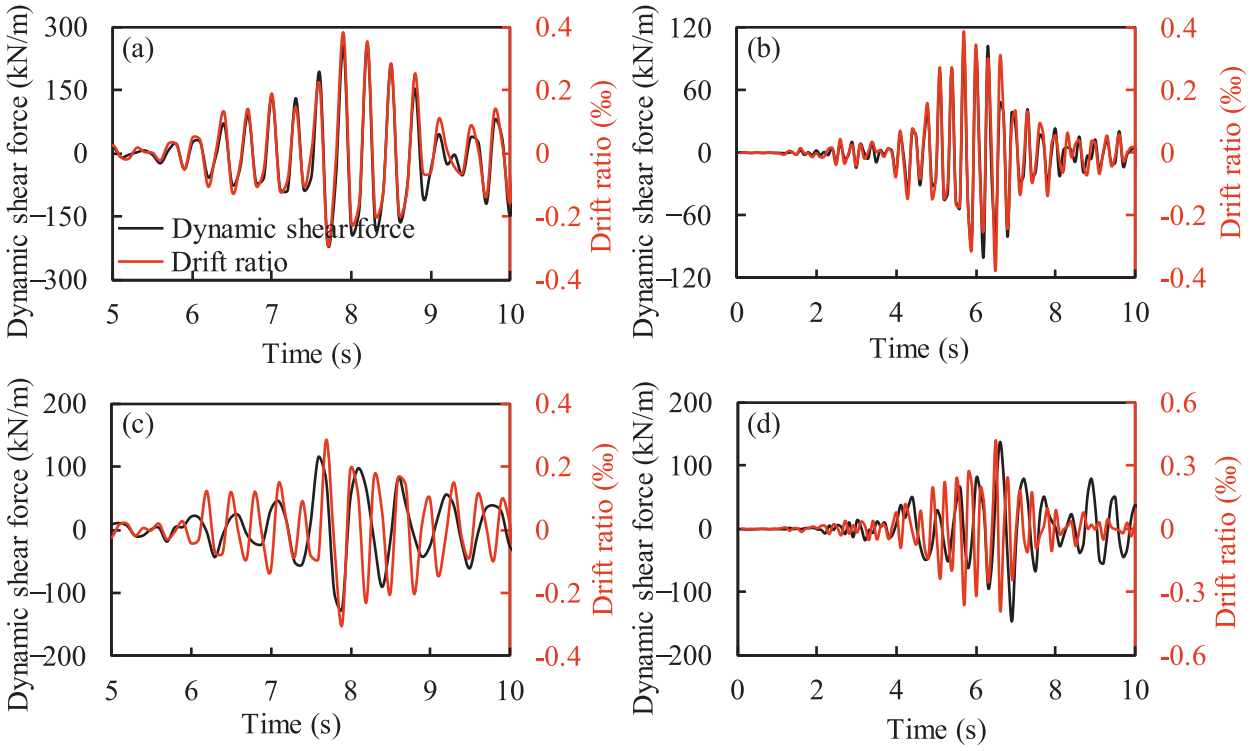

Fig. 11. Time history of underground structure drift ratio and dynamic shear force at the base of the aboveground structure. (a) 5-story aboveground structure under G2, (b) 5-story aboveground structure under G4, (c) 10-story aboveground structure under G2, and (d) 10-story aboveground structure under G4.

and settlement of the underground structure under different input motions. A positive vertical displacement means uplift, while a negative vertical displacement means settlement. The simulations without the aboveground structure show uplift under all five input motions. This is because the weight of the underground structure is smaller than that of the soil it replaces, being 58.5 and 108 t/m, respectively, causing the underground structure to uplift when the soil liquefies. When aboveground structure exists, settlement is observed, as the weight of the aboveground structure plus the underground structure exceeds that of the soil, being 112.7, 167.0, and 221.3 t/m for the 5, 10, and 15-story cases, respectively.

There are also significant differences in the vertical displacement under different input motions. Figure 12(b) shows the liquefaction depth at the bottom of the underground structure for different cases and input motions, indicating that for the same aboveground structure, the amplitude of uplift or settlement of the underground structure is clearly associated with the liquefaction of the soil. For instance, G3, which has the greatest CAV, also exhibits the greatest liquefaction depth and vertical displacement.

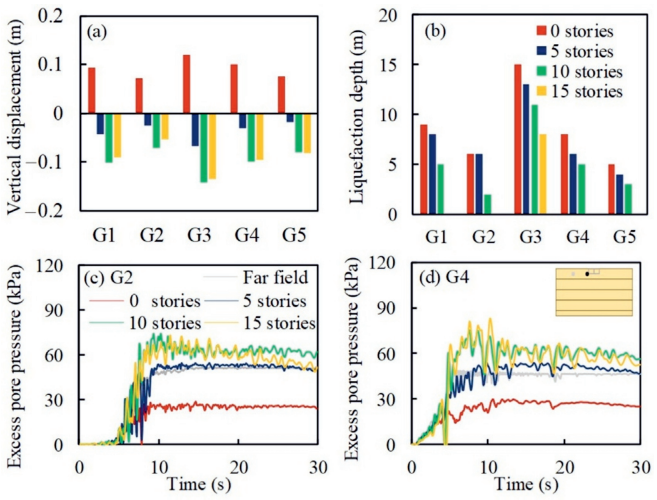

Fig. 12. Vertical displacement, liquefaction depth, and excess pore pressure in the elastoplastic simulations. (a) Vertical displacement at the bottom of the central column under different input motions, (b) liquefaction depth below the underground structure under different input motions, (c) excess pore pressure of far field and near structure at a depth of 5 m under G2, and (d) excess pore pressure of far field and near structure at a depth of 5 m under G4.

A similar trend is observed between G4 and G5, where greater CAV corresponds to larger liquefaction depth and vertical displacement. Interestingly, G1 and G2, despite having lower CAV than G5, result in greater liquefaction depth and vertical displacement. This suggests that liquefaction is a key factor influencing vertical displacement.

To evaluate the influence of the aboveground structure, Fig. 12(c) and (d) further shows the excess pore pressure time history in the far field and near structure at a depth of 5 m under G2 and G4. Although increasing structural height and weight reduce the liquefaction depth, the accumulation of excess pore pressure continues to rise. Under different input motions, the excess pore pressure in soil for the 5-story case is consistently lower than that for the 10-story case, while the excess pore pressures for the 10- and 15-story cases are similar. This trend indicates a positive correlation between the excess pore pressure and the vertical displacement of underground structure, which is directly associated with the change in effective stress in soil beneath the structure caused by the seismic event.

4 Simplified analysis method for underground structure seismic response in IUASS

4.1 Simplified analysis method for drift ratio

The previous analysis shows that the forces imposed by the aboveground structure at its base have a strong linear correlation with the drift ratio of the underground structure. These forces should thus be considered in developing a simplified analysis method for the drift ratio of the underground structure within an IUASS. The forces can be calculated with various simplified methods, such as the mode-superposition response spectrum and the bottom shearing force method (International Organization for Standardization, 2017; MOHURD, 2010). At the same time, various simplified methods exist for calculating the drift ratio of underground structures. These two types of methods can be combined to propose a simplified method for the drift ratio of underground structures in IUASS.

In combining these two methods, one issue that must be resolved is whether the peak inertia effect from the aboveground structure should be directly summed with the peak kinematic effect from the soil. Figure 11 clearly indicates that this is not always the case, and the peak force at the base of the aboveground structure may not occur simultaneously with the peak underground structure drift ratio. Another issue that should be considered is the influence of soil–structure interaction, especially when using simplified analysis methods for the aboveground structure that assume its foundation to be rigid. This may result in an underestimation of the forces imposed by aboveground structure using simplified analysis methods compared to the dynamic analysis method, particularly in soft soil conditions (Wu et al., 2025). Therefore, a simplified method should take these into consideration when applying the base forces of the aboveground structure to the underground structure.

A simplified method for the drift ratio of underground structure in IUASS, appropriately accounting for the forces imposed by aboveground structure, is proposed in this study. The force imposed by the aboveground structure is calculated using the mode-superposition response spectrum method, which considers the fundamental period of the aboveground structure and the mean period of the input motion, while the drift ratio of the underground structure is calculated using the displacement-based pseudo static method, which accounts for the characteristics of the input motion. The modification of the force imposed by the aboveground structure force is also taken into careful consideration. The proposed method can be summarized as the following 5 steps:

(1) Conduct modal analysis to obtain the first three fundamental periods of the aboveground structure T_1, T_2, T_3, and displacement modes of the aboveground structure X_{1i}, X_{2i}, X_{3i}, as well as the fundamental periods of the free field T_f and the structure–soil system T_{total}.
(2) Conduct dynamic free field analysis to determine the maximum ground acceleration a_{max}, as well as the soil acceleration a_i, displacement d_i, and shear stress τ_i at the moment of maximum drift of the underground structure. Determine the subgrade coefficient K_s. This subgrade coefficient K_s is derived by applying a unit force F at the target location.
(3) Obtain the maximum horizontal response spectra ratio α_{max} with the following equation:

$$\alpha_{max} = a_{max}/g, \tag{14}$$

where a_{max} is the maximum ground acceleration from free field analysis, and g is the gravity acceleration. Calculate the original forces S_{EK} imposed by the aboveground structure at the base using the mode-superposition response spectrum method with the following equations:

$$S_{EK} = \sqrt{\sum_{j=1}^{m}\left(\sum_{i=1}^{n} F_{ji}\right)^2}, \tag{15}$$

$$F_{ji} = \alpha_j X_{ji} G_i \sum_{i=1}^{n} X_{ji} G_i / \sum_{i=1}^{n} X_{ji}^2 G_i, \tag{16}$$

where α_j is the horizontal seismic coefficient of jth mode calculated with the curve in Fig. 13, and G_i is the gravity load of the ith story.

(4) Modify the computed forces S_{EK} using the proposed equations:

$$S_{EKM} = \eta S_{EK}, \tag{17}$$

$$\eta = \begin{cases} \max\left(\gamma\left(\frac{T_{total}}{T_1} - \frac{1}{2}\right), 1\right), & \text{if } T_m < T_f \\ \sqrt{T_f/T_{total}}, & \text{if } T_m \geq T_f \end{cases}, \tag{18}$$

where γ is an empirical parameter with $\gamma = 1.2$, based on the case studies in this paper. When $T_m < T_f$ and the aboveground structure is low, an amplification factor of $\max(\gamma(T_{total}/T_1 - 1/2), 1)$ is applied. Here, the ratio T_{total}/T_1 increases as the aboveground structure height decreases. When $T_m \geq T_f$, a reduction factor of $(T_f/T_{total})^{0.5}$ is introduced, where T_f/T_{total} is always smaller than 1. The ratio T_f/T_{total} increases as the aboveground structure height decreases.

The modification considers the influence of both the possible phase difference between the aboveground structure base force and the drift ratio of the underground structure, and soil–structure interaction. Since soil–structure interaction effect is more pronounced and significant in soft soil conditions (when the free field fundamental period T_f is relatively large), the modification is determined by the relative relationship between the input motion mean period T_m and the free field fundamental period T_f. When $T_m < T_f$,

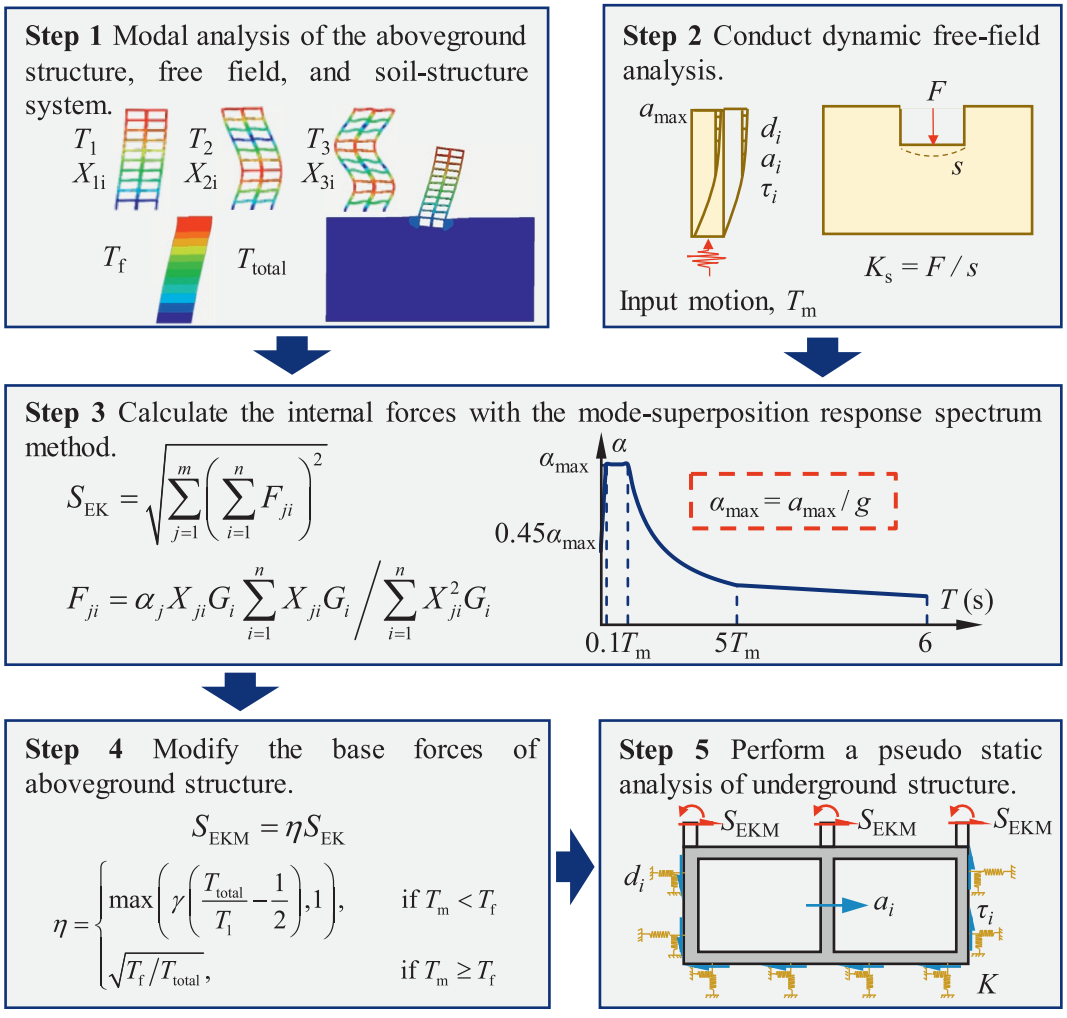

Fig. 13. Flowchart of the proposed 5-step simplified analysis method to obtain the drift ratio of the underground structure in IUASS.

the forces imposed by the aboveground structure are amplified. When $T_m \geq T_f$, the force imposed by the aboveground structure is reduced.

(5) Perform a displacement-based pseudo static analysis of the underground structure, and obtain its drift ratio.

Figure 14 presents the drift ratios calculated by the proposed simplified analytical method compared with the results from dynamic analysis, showing good agreement for different aboveground structure heights and input motions, with R^2 of 0.87 and 0.89 for the linear elastic and elastoplastic simulations, respectively. It should be noted that the parameter γ adopted in this study is only a recommended value based on the given soil conditions, and its applicability under different soil conditions requires further study.

The effect of the modified equation introduced in Step 4 is further evaluated. Figure 15 shows the drift ratio calculated without applying the modification in Step 4. Although the overall slopes without modification are only slightly different for the elastic and elastoplastic cases, the R^2 are significantly lower compared with the results obtained after modification, being only 0.68 and 0.63 for the elastic and elastoplastic cases, respectively. In Fig. 15 (c) and (d), significant underestimation is observed for low aboveground structure (5-story) under G2, where $T_m < T_f$, resulting from the effect of soil–structure interaction. Significant overestimation is observed for tall aboveground structures (10- or 15-story) under G4, where $T_m \geq T_f$, resulting from the effect of the phase difference between peak base forces and peak drift ratio. These results highlight the need for the modifications proposed in Step 4.

A simple parameter sensitivity analysis is conducted for the empirical parameter γ as shown in Fig. 16. When γ varies from 1.0 to 1.4, R^2 remains unchanged, while the average ratio increases from 1.03 to 1.21. The results show that small variations in the values of γ have a limited effect on the correlation quality but can cause the simplified analysis results to be either systematically larger or smaller. The proposed γ is only a suggested value for the cases in this study, and the calibration of a more reasonable value for more general cases requires further research.

4.2 Simplified analysis method for vertical displacement

For the vertical displacement of the underground structure, it is observed that when the mass of the IUASS is less than that of the free field replaced by the underground structure, uplift occurs relative to the free field. When the mass of the IUASS is greater, relative settlement occurs. In other words, when the total mass m_s of the IUASS is smaller than the free field mass m_f of the volume replaced by the underground structure, relative uplift occurs; when $m_s > m_f$, relative settlement occurs.

Besides the mass of structure, the results in Section 3.3 show that input motion and excess pore pressure development significantly influence vertical displacement. Considering these two factors, a simplified analysis method is proposed, which introduces the influence of input motion via free field dynamic analysis, and computes the vertical displacement of the structure using the excess pore pressure obtained in free field analysis. The proposed simplified method follows 3 steps, as shown in Fig. 17:

(1) Conduct free field dynamic analysis to obtain the distribution of excess pore pressure (EPP) p_i along depth and surface settlement s_f.
(2) Locate depth h_2 in the free field, where the initial vertical effective stress is the same as that at the base of the underground structure at h_1. Shift the distribution of excess pore pressure p_i vertically by h_2–h_1 to obtain a modified EPP distribution. The difference Δp_i between these two distributions is calculated.
(3) Compute the vertical displacement relative to the free field using the layer-wise summation method. The

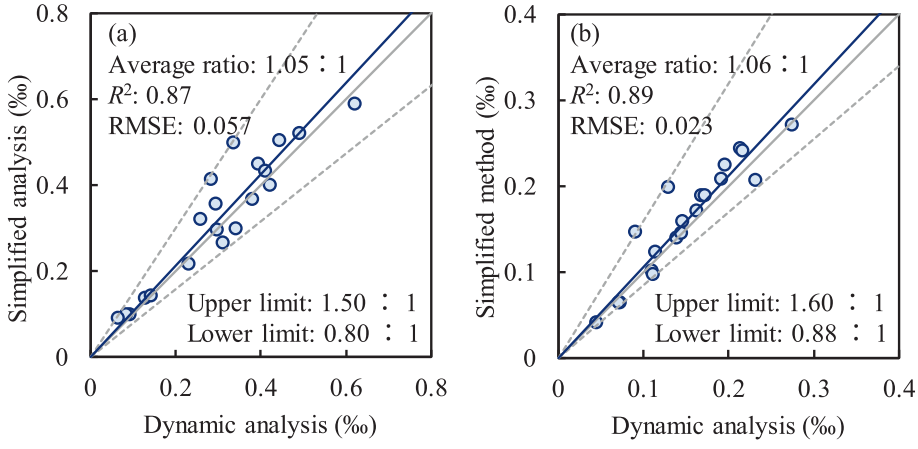

Fig. 14. Comparison of the drift ratio calculated by the simplified analysis method and the dynamic analysis method. (a) Linear elastic simulation, and (b) elastoplastic simulation.

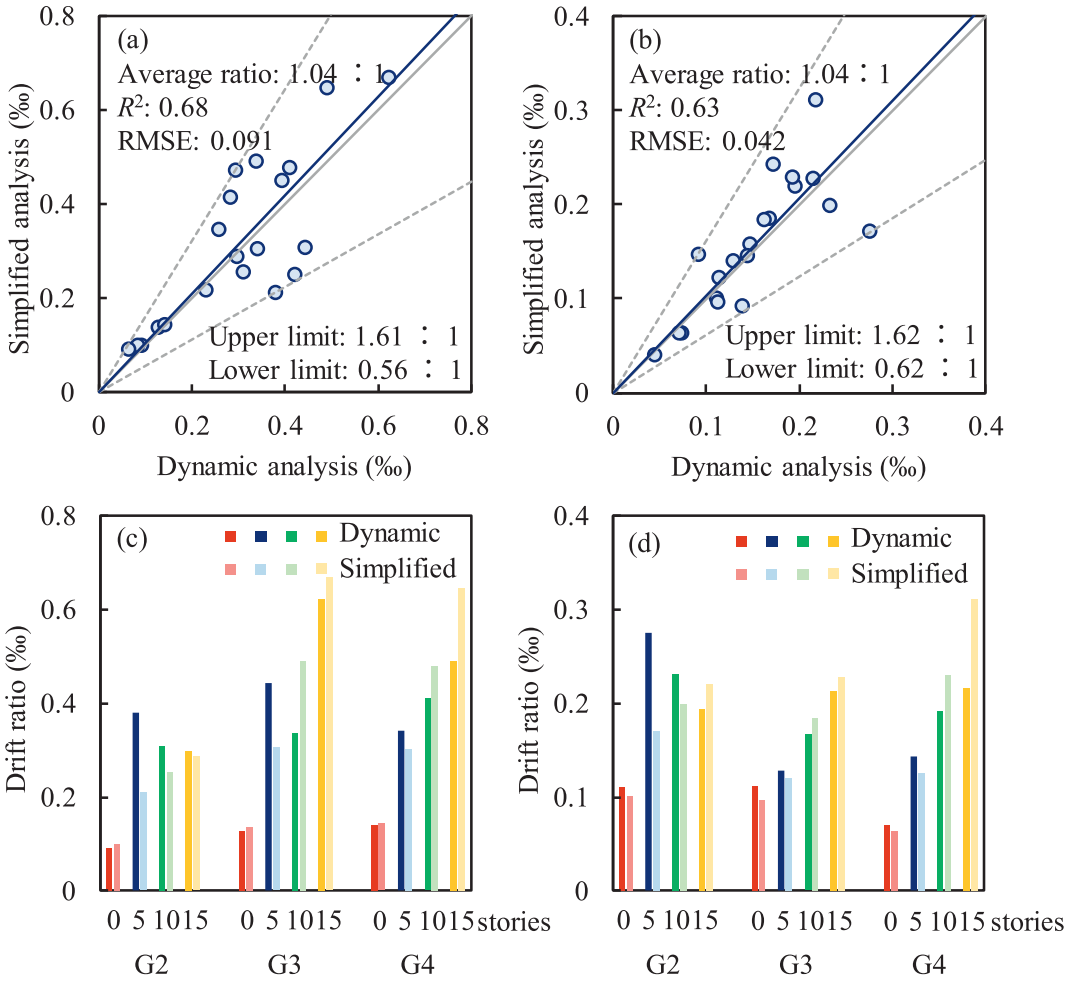

Fig. 15. Comparison of the drift ratio calculated by the simplified analysis method without Step 4 modification and the dynamic analysis method. (a) Linear elastic simulation, (b) elastoplastic simulation, (c) linear elastic simulation under G2, G3, and G4, and (d) elastoplastic simulation under G2, G3, and G4.

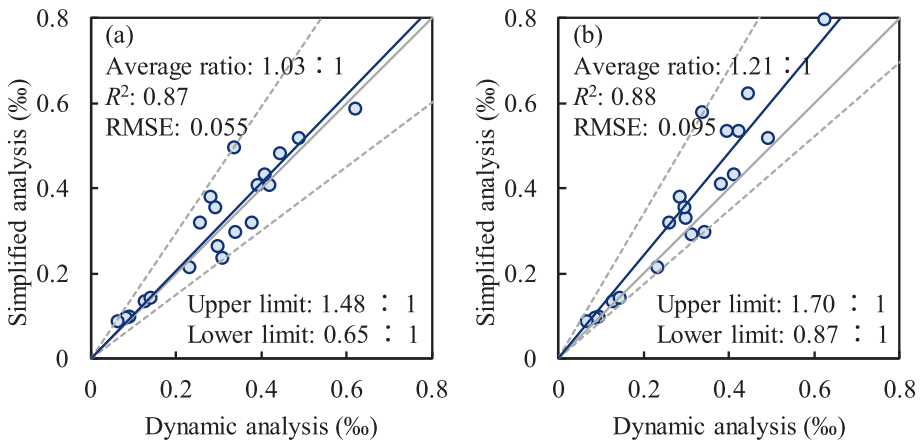

Fig. 16. Comparison of the drift ratio calculated by the simplified analysis method and the dynamic analysis method: (a) $\gamma = 1.0$, and (b) $\gamma = 1.4$.

compression modulus can be calculated with the bulk modulus and Poisson's ratio. The calculated relative vertical displacement is then modified and added to the free field surface displacement s_f to obtain the total vertical displacement, as expressed in the following equations:

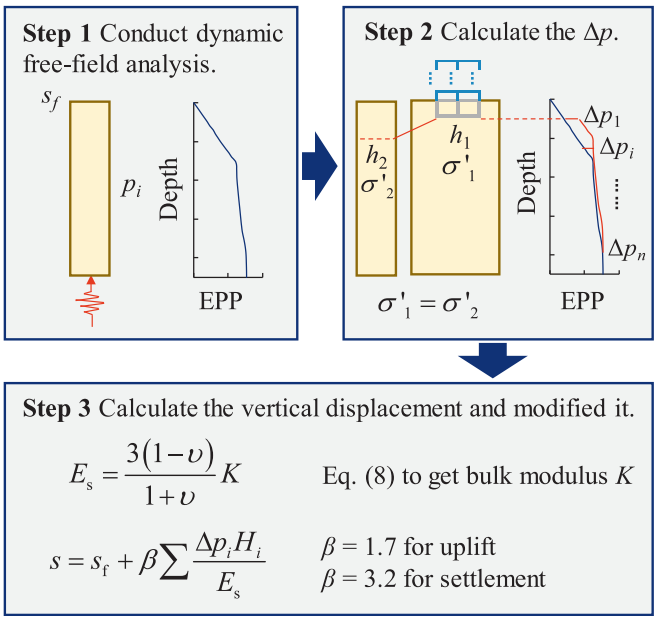

Fig. 17. Flowchart of the 3-step simplified analysis method to analyze the vertical displacement of the underground structure in IUASS.

$$E_s = \frac{3(1-\upsilon)}{1+\upsilon} K, \tag{20}$$

$$s = s_f + \beta \sum \frac{\Delta p_i H_i}{E_s}, \tag{21}$$

where E_s is the compression modulus, v is the Poisson's ratio, K is the bulk modulus, which can be calculated with Eq. (8), s is the total vertical displacement, H_i is the height of each layer in the layer-wise summation method, and β is the modified coefficient, which is obtained empirically to be 1.7 for uplift and 3.2 for settlement.

This method assumes that the vertical displacement of the underground structure results from the difference in excess pore pressure between the near field and far field. To efficiently estimate the excess pore pressure of the near field, the pore pressure distribution is vertically shifted by h_2–h_1. The mechanical rationale for this shift is based on comparing excess pore pressures under identical initial vertical effective stress conditions. The depth h_2 in the free field is defined as the depth where the initial vertical effective stress equals that in the near field at a depth of h_1. This shift accounts for the weight of the structure itself, providing a straightforward adaptation method for applying the free-field response to estimate the excess pore pressure in the near field.

The results of the simplified analysis method are shown in Fig. 18 against the dynamic analysis results. The average ratio between the two sets of results is 1.09, with an R^2 of 0.97, indicating that the proposed simplified analysis method agrees well with the dynamic analysis method for all the cases. Additionally, it only requires performing the free field dynamic analysis, making it relatively easy to implement in practice. The only requirement of the method is that the free field dynamic analysis must employ a solid–fluid coupled method and adopt a soil constitutive model that can appropriately simulate excess pore pressure development. It should be noted that the parameter β adopted in this paper is only a recommended value based on the given soil conditions, and its applicability under different soil conditions requires further study.

A simple parameter sensitivity analysis is conducted for the empirical parameter β as shown in Fig. 19. When $\beta = 1.5/3$, the average ratio is exactly 1.00, and when $\beta = 1.8/3.4$, the average ratio increases to 1.14, while the R^2 remains unchanged. The results show that small variations in β have a limited effect on the correlation quality but can cause the simplified analysis results to be either systematically larger or smaller. The proposed β is only a suggested value for the cases in this study, and the calibration of a more reasonable value for more general cases requires further research.

4.3 Validation of the proposed simplified methods

To validate the proposed simplified analysis methods for drift ratio and vertical displacement, an additional 17 cases were analyzed, as shown in Table 4. Cases No. 5 and 6 employ 3 additional input motions while adopting both linear elastic and elastoplastic simulations. Cases No. 7–10 use input motion G2 and G3 to investigate the influence of mass and stiffness of the aboveground structure using linear elastic analysis. Case No. 11 adopts a 4-story aboveground structure. Cases No. 12 and 13 adopt different PGAs in both linear elastic and elastoplastic simulations. The 3 additional input motions G6, G7, and G8 are shown in Fig. 20. Note that G8 has a significantly greater period compared to the ones in Fig. 3, with $T_m = 1.01$ s.

Figure 21 presents the drift ratio results for the validation cases. The average ratio between the simplified analysis method results and dynamic analysis results is 1.02:1, with an R^2 of 0.90, indicating good agreement. Figure 21 (b) shows the results under G8, G2, and G4 in more detail. These results confirm that the proposed simplified analysis method can effectively evaluate the drift ratio of underground structures under a wide range of input motion mean period, PGA, and aboveground structure mass and stiffness.

For the validation of the simplified analysis method for vertical displacement, the judgement for uplift or settlement is first assessed for Case No. 11 with 4-story aboveground structure under G2. Figure 22(a) shows the vertical displacements at the ground surface for the 4-story case and 5-story case (Case No. 2 in Table 2). The vertical displacement of the far field is also provided, showing 1.6 cm of settlement. The 5-story case results in 2.6 cm settlement, while the 4-story case demonstrates significantly reduced settlement of only 0.2 cm, resulting in relative uplift compared to the free field. This is because the structure mass of 101.9 t/m is slightly smaller than the replaced soil of 108 t/m. The simulation results agree with the uplift

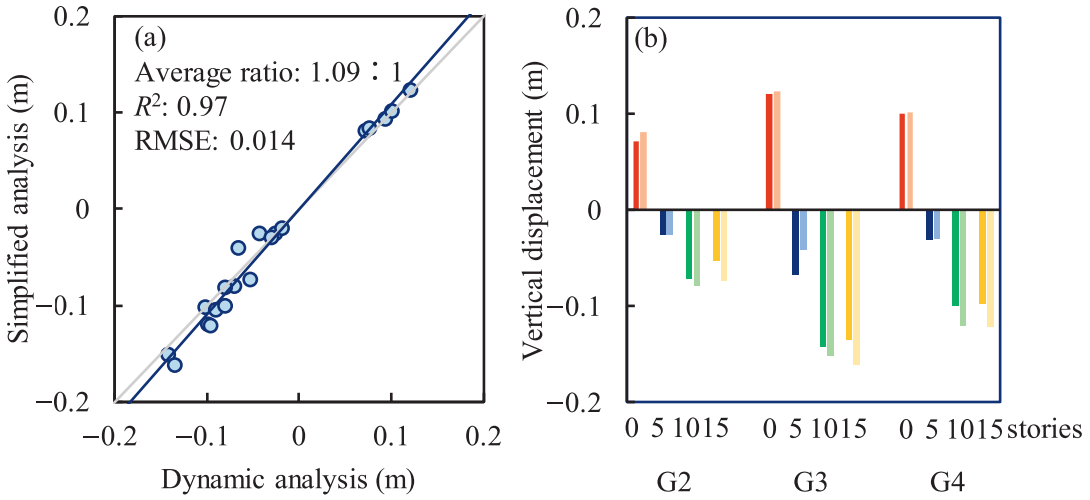

Fig. 18. Comparison of the vertical displacement calculated by the simplified analysis method and the dynamic analysis method. (a) All 20 simulation cases, and (b) under G2, G3, and G4.

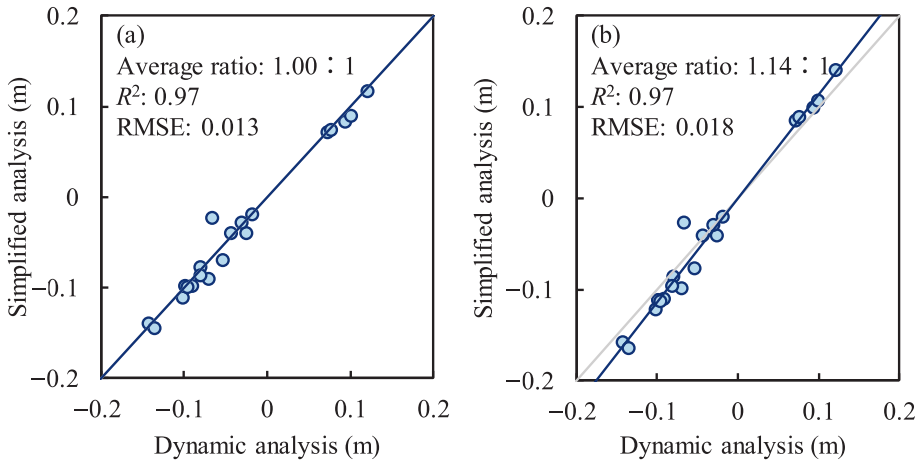

Fig. 19. Comparison of the vertical displacement calculated by the simplified analysis method and the dynamic analysis method: (a) $\beta = 1.5/3.0$, and (b) $\beta = 1.8/3.4$.

Table 4
Validation cases with different input motions and numbers of aboveground structure stories.

Case No.	Input motion	Linear elastic or elastoplastic	Aboveground structure stories	Other information
5	G6, G7, G8	Both	5	–
6	G6, G7, G8	Both	10	–
7	G2, G3	Linear elastic	10	Half mass for aboveground structure
8	G2, G3	Linear elastic	10	Twice the mass for aboveground structure
9	G2, G3	Linear elastic	10	Half stiffness for aboveground structure
10	G2, G3	Linear elastic	10	Twice the stiffness for aboveground structure
11	G2	Elastoplastic	4	–
12	G4	Both	10	PGA = 0.1g
13	G4	Both	10	PGA = 0.3g

and settlement criterion proposed for the simplified method.

The simplified method to calculate the vertical displacement is assessed using Cases No. 5, 6, and 11–13 using the elastoplastic simulation. Figure 22(b) compares the vertical displacements obtained from dynamic analysis and the simplified analysis method for these cases. This result showcases that the proposed simplified analysis method

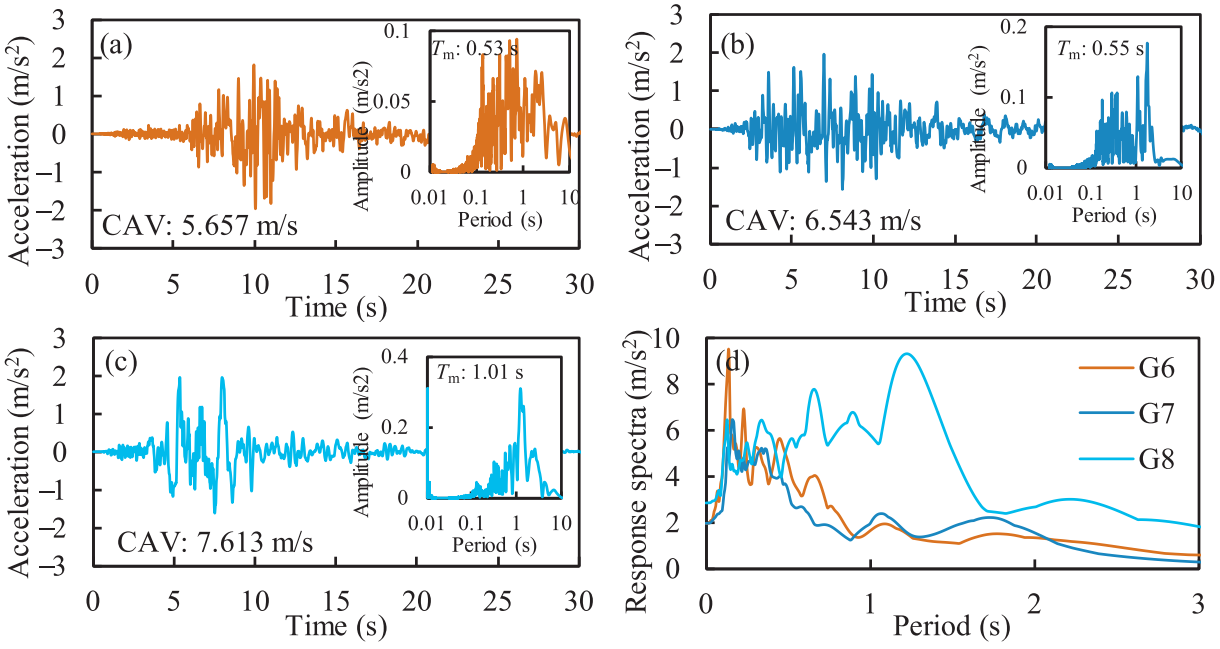

Fig. 20. Additional seismic input motions for validation in the simulations and their Fourier amplitude and response spectra: (a) G6 Imperial Valley, (b) G7 Kobe, (c) G8 KBU, and (d) response spectra for G6, G7, and G8.

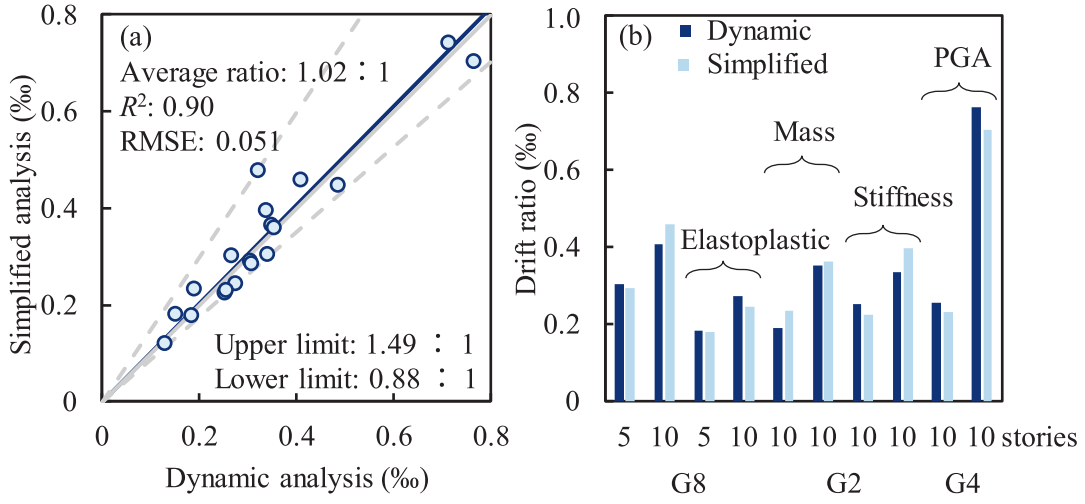

Fig. 21. Comparison of the drift ratio calculated by the simplified analysis method and the dynamic analysis method. (a) All validation cases, and (b) validation cases of G8, G2, and G4.

achieves good prediction of underground structure vertical displacement for different input motions and aboveground structure conditions.

5 Conclusions

This study conducts linear elastic and elastoplastic dynamic simulations to analyze the drift ratio and vertical displacement of the underground structure within an IUASS under seismic loading. Based on the patterns obtained from the dynamic analysis, simplified analysis methods for drift ratio and vertical displacement prediction are proposed for the underground structure in an IUASS. The main findings are summarized as follows:

(1) The mean period of input motion and the fundamental period of the structure system significantly affect the drift ratio of the underground structure. When the mean period of input motion is greater than the fundamental period of the free field, an increase in aboveground structure height increases the drift ratio of the underground structure. When the mean period of input motion is smaller than the fundamental period of the free field, an increase in aboveground struc-

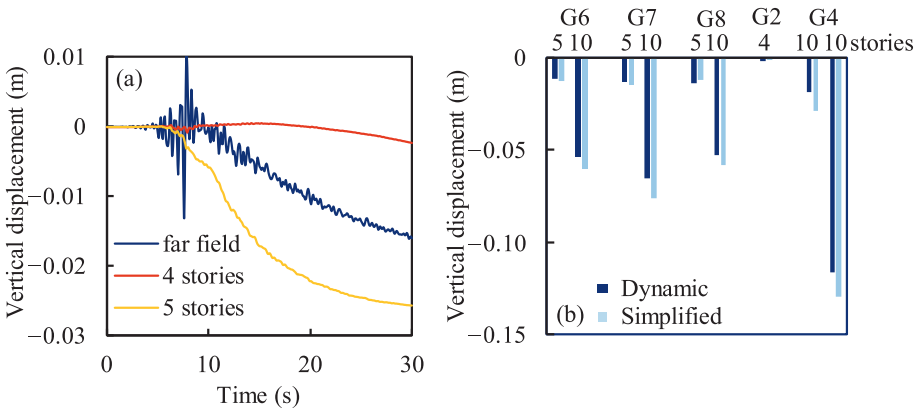

Fig. 22. Vertical displacement in dynamic simulation and simplified analysis method. (a) Comparison of the vertical displacement of far field and underground structure with different numbers of aboveground structure stories, and (b) comparison of the settlement calculated by the simplified analysis method and the dynamic analysis method.

ture height could reduce the drift ratio of underground structure, as the motion of the aboveground structure becomes out of phase with that of the underground structure. The dynamic simulation results also reveal a strong correlation between the forces at the base of the aboveground structure and the drift ratio of the underground structure.

(2) The weight of the structure and input motion significantly affect the vertical displacement of the underground structure. When the weight of IUASS is less than that of the soil replaced by the underground structure, uplift relative to the free field is observed. When the weight of IUASS exceeds that of the soil replaced by the underground structure, settlement occurs. Elastoplastic dynamic simulation results reveal a strong correlation between the vertical displacement of the underground structure and the excess pore pressure in the soil.

(3) A simplified calculation method for the drift ratio of underground structures in an IUASS is proposed. The proposed method applies a force from the aboveground structure base to the underground structure in the displacement-based pseudo static analysis method to determine the drift ratio. A key procedure is that the force from the aboveground structure is modified from the base force obtained using the mode-superposition response spectrum method, with the modification accounting for the influence of the mean period of input motion and the fundamental period of the aboveground structure.

(4) A simplified calculation method for the vertical displacement of underground structures is also proposed. Uplift or settlement is first determined by comparing the weight of the IUASS with the weight of the soil replaced by the underground structure. The vertical displacement value is then calculated via the layer-wise summation method by considering the near field excess pore pressure increment compared to the free field generated during shaking under the influence of the IUASS.

(5) The proposed simplified methods are shown to be able to accurately predict the drift ratio and vertical displacement of the underground structure for the 40 dynamic simulation cases used to analyze the system response pattern. More importantly, another 21 cases that expand the range of input motion and aboveground structure characteristics are simulated and used to further independently validate the simplified methods, showing excellent agreement between predicted and dynamic simulation results for both drift ratio and vertical displacement over a wide range of conditions.

It should be noted that the proposed simplified methods are validated against numerical simulations in this study. Future experimental studies should be conducted to further validate and possibly improve the methods, as all numerical simulations are under a 2D plane strain condition. A wider range of soil conditions should also be considered in future studies.

Data availability

The data that support the findings of this study are available from the corresponding author upon reasonable request.

CRediT authorship contribution statement

Jia-Ke Yu: Writing – original draft, Investigation, Data curation. **Jun-Guang Huang:** Writing – review & editing. **Meng-Xiong Tang:** Writing – review & editing. **Jian-Min Zhang:** Writing – review & editing. **Rui Wang:** Writing – review & editing, Methodology, Conceptualization.

Declaration of competing interest

The authors declare that they have no known competing financial interests or personal relationships that could have appeared to influence the work reported in this paper.

Acknowledgement

The authors would like to thank the National Natural Science Foundation of China (Grant Nos. 52378349 and 52425904) for funding this study.

References

Azadi, M., & Hosseini, S. M. M. (2010). The uplifting behavior of shallow tunnels within the liquefiable soils under cyclic loadings. *Tunnelling and Underground Space Technology, 25*(2), 158–167.

Bao, X., Xia, Z., Ye, G., Fu, Y., & Su, D. (2017). Numerical analysis on the seismic behavior of a large metro subway tunnel in liquefiable ground. *Tunnelling and Underground Space Technology, 66*, 91–106.

Been, K., & Jefferies, M. G. (1985). A state parameter for sands. *Géotechnique, 35*(2), 99–112.

Bélanger, P. (2007). Underground landscape: The urbanism and infrastructure of Toronto's downtown pedestrian network. *Tunnelling and Underground Space Technology, 22*(3), 272–292.

Bhalla, S., Yang, Y., Zhao, J., & Soh, C. (2005). Structural health monitoring of underground facilities–Technological issues and challenges. *Tunnelling and Underground Space Technology, 20*(5), 487–500.

Chen, G., Chen, S., Qi, C., Du, X., Wang, Z., & Chen, W. (2015). Shaking table tests on a three-arch type subway station structure in a liquefiable soil. *Bulletin of Earthquake Engineering, 13*, 1675–1701.

Chen, R. R., Taiebat, M., Wang, R., & Zhang, J. M. (2018). Effects of layered liquefiable deposits on the seismic response of an underground structure. *Soil Dynamics and Earthquake Engineering, 113*, 124–135.

Cui, C., Xu, M., Xu, C., Zhang, P., & Zhao, J. (2023). An ontology-based probabilistic framework for comprehensive seismic risk evaluation of subway stations by combining Monte Carlo simulation. *Tunnelling and Underground Space Technology, 135*, 105055.

Cui, C., Zhao, J., Xu, M., Xu, C., Liu, H., & Wang, K. (2025). Multidimensional seismic fragility analysis of subway station structures using the adaptive bandwidth kernel density estimation and Copula function. *Underground Space, 22*, 110–123.

Fu, P. C., Johnson, S. M., & Carrigan, C. R. (2013). An explicitly coupled hydro-geomechanical model for simulating hydraulic fracturing in arbitrary discrete fracture networks. *International Journal for Numerical and Analytical Methods in Geomechanics, 37*(14), 2278–2300.

China Ministry of Natural Resources. (2020). *Recommended directory of comprehensive development modes of aboveground-underground space of rail transits*. Beijing (in Chinese).

Gillis, K., Dashti, S., Hashash, Y. M. A., Jones, C., Musgrove, M., & Walker, M. (2015). Seismic performance of shallow underground structures adjacent to tall buildings: a centrifuge experimental study. In: *Proceedings of the 6th International Conference on Earthquake Geotechnical Engineering*, Christchurch, New Zealand.

Hashash, Y. M. A., Hook, J. J., Schmidt, B., John, I., & Yao, C. (2001). Seismic design and analysis of underground structures. *Tunnelling and Underground Space Technology, 16*(4), 247–293.

Hashash, Y. M. A., Dashti, S., Musgrove, M., Gillis, K., Walker, M., Ellison, K., & Basarah, Y. I. (2018). Influence of tall buildings on seismic response of shallow underground structures. *Journal of Geotechnical and Geoenvironmental Engineering, 144*(12), 04018097.

He, B., Zhang, J. M., Li, W., & Wang, R. (2020). Numerical analysis of LEAP centrifuge tests on sloping liquefiable ground: Influence of dilatancy and post-liquefaction shear deformation. *Soil Dynamics and Earthquake Engineering, 137*, 106288.

He, W. (2011). *Research on seismic response of underground structures and its interaction with ground building* [Doctoral dissertation, Dalian University of Technology]. China Science Periodical Database (in Chinese).

Hu-Yan, B., Wang, R., Yu, J. K., & Zhang, J. M. (2024). Predictions of seismic response for sheet-pile wall in liquefiable deposit within LEAP 2022 using the CycLiq constitutive model. *Soil Dynamics and Earthquake Engineering, 178*, 108474.

Iida, H., Hiroto, T., Yoshida, N., & Iwafuji, M. (1996). Damage to Daikai subway station. *Soils and Foundations, 36*(Special), 283–300.

International Organization for Standardization (2017). Bases for design of structures — Seismic actions on structures. *ISO, 3010*, 2017.

Iwatate, T., Kobayashi, Y., Kusu, H., & Rin, K. (2000). *Investigation and shaking table tests of subway structures of the Hyogoken-Nanbu earthquake*. New Zealand: New Zealand Society for Earthquake Engineering.

Kramer, S. L., & Mitchell, R. A. (2006). Ground motion intensity measures for liquefaction hazard evaluation. *Earthquake Spectra, 22*(2), 413–438.

Li, W. T., Wang, R., & Zhang, J. M. (2023). Influence of aboveground structure on connected underground structure seismic response within an integrated system. *Tunnelling and Underground Space Technology, 134*, 105003.

Li, Y., Wang, R., Ma, H., & Zhang, J. M. (2025). Rising groundwater table due to restoration projects amplifies earthquake induced liquefaction risk in Beijing. *Nature Communications, 16*, 1466.

Li, Y. Y., Zhang, J. M., & Wang, R. (2024). An explicit material point and finite volume sequentially coupled method for simulating large deformation problems in saturated soil. *Computers and Geotechnics, 170*(6), 1–20.

Liu, B., Zhang, D., Li, X., & Li, J. (2022a). Seismic response of underground structure–soil–aboveground structure coupling system: Current status and future prospects. *Tunnelling and Underground Space Technology, 122*, 104372.

Liu, J., Zhu, T., Wang, R., & Zhang, J. M. (2022b). A simplified seismic analysis method for underground structures considering the effect of adjacent aboveground structures. In *Conference on Performance-based Design in Earthquake. Geotechnical Engineering* (pp. 2313–2321). Cham: Springer International Publishing.

Ma, C. X., Peng, F. L., Qiao, Y. K., & Li, H. (2022). Evaluation of spatial performance of metro-led urban underground public space: A case study in Shanghai. *Tunnelling and Underground Space Technology, 124*, 104484.

Ministry of Housing and Urban-Rural Development of the People's Republic of China. (2010). *Code for seismic design of buildings* (GB 50011—2010). China Architecture & Building Press: Beijing (in Chinese).

Pitilakis, K., & Tsinidis, G. (2013). Performance and seismic design of underground structures. In *Earthquake geotechnical engineering design* (pp. 279–340). Cham: Springer International Publishing.

Pitilakis, K., Tsinidis, G., Leanza, A., & Maugeri, M. (2014). Seismic behaviour of circular tunnels accounting for aboveground structures interaction effects. *Soil Dynamics and Earthquake Engineering, 67*, 1–15.

Qiu, D., Wang, P., Ren, W., Chen, J., & Zhao, C. (2023). Seismic responses and failure mechanism of the superstructure-integrated underground structure considering the seismic aboveground-underground interaction. *Soil Dynamics and Earthquake Engineering, 175*, 103259.

Qiu, Y. J., Zhang, H. R., Yu, Z. Y., & Zhang, J. K. (2021). A modified simplified analysis method to evaluate seismic responses of subway stations considering the inertial interaction effect of adjacent buildings. *Soil Dynamics and Earthquake Engineering, 150*, 106896.

Ramazi, H., & Jigheh, H. S. (2006). The Bam (Iran) Earthquake of December 26, 2003: From an engineering and seismological point of view. *Journal of Asian Earth Sciences, 27*(5), 576–584.

Rashiddel, A., Abedi, M., Dias, D., & Ramesh, A. (2024). Seismic analysis of segmental shallow tunnels adjacent to building foundations under soil liquefaction and its mitigation. *Soil Dynamics and Earthquake Engineering, 178*, 108479.

Rathje, E. M., Abrahamson, N. A., & Bray, J. D. (1998). Simplified frequency content estimates of earthquake ground motions. *Journal of Geotechnical and Geoenvironmental Engineering, 124*(2), 150–159.

Scarfone, R., Morigi, M., & Conti, R. (2020). Assessment of dynamic soil-structure interaction effects for tall buildings: A 3D numerical approach. *Soil Dynamics and Earthquake Engineering, 128*, 105864.

Stewart, J. P., Fenves, G. L., & Seed, R. B. (1999). Seismic soil-structure interaction in buildings. I: Analytical methods. *Journal of Geotechnical and Geoenvironmental Engineering, 125*(1), 26–37.

Wang, G. B., Yuan, M. Z., Miao, Y., Wu, J., & Wang, Y. X. (2018). Experimental study on seismic response of underground tunnel-soil-

surface structure interaction system. *Tunnelling and Underground Space Technology, 76*, 145–159.

Wang, R., Liu, H., Kutter, B. L., & Zhang, J. M. (2023). Influence of centrifuge test soil-container friction on seismic sheet-pile wall response in liquefiable deposit: Insights from numerical simulations. *Journal of Geotechnical and Geoenvironmental Engineering, 149*, 04023068.

Wang, R., Zhang, J. M., & Wang, G. (2014). A unified plasticity model for large post-liquefaction shear deformation of sand. *Computers and Geotechnics, 59*, 54–66.

Wang, R., Zhu, T., Yu, J. K., & Zhang, J. M. (2022). Influence of vertical ground motion on the seismic response of underground structures and underground-aboveground structure systems in liquefiable ground. *Tunnelling and Underground Space Technology, 122*, 104351.

Ministry of Housing and Urban-Rural Development of the People's Republic of China. (2018). *Standard for seismic design of underground structure* (GB/T 51336—2018). China Architecture & Building Press: Beijing. (in Chinese).

Wang, R. X. (2020). *Research on fluid-solid coupling analysis and visualization method for large-scale geotechnical engineering problems*. [Doctoral dissertation, Tsinghua University]. Tsinghua University Library (in Chinese).

Wu, Y., Zhao, M., Gao, Z., et al. (2025). Response spectrum method for seismic analysis of aboveground structure based on effective frequencies and modes of soil-structure interaction system. *Soil Dynamics and Earthquake Engineering, 196*, 109485.

Xu, Z. G., Du, X. L., Xu, C. S., Jiang, J., & Han, R. (2019). Simplified equivalent static methods for seismic analysis of shallow buried rectangular underground structures. *Soil Dynamics and Earthquake Engineering, 121*, 1–11.

Xu, M., Cui, C., Xu, C., Zhang, P., & Zhao, J. (2023a). Seismic risk analysis of subway station structures combining the epistemic uncertainties from both seismic hazard and numerical simulation. *Journal of Earthquake Engineering, 28*(5), 1474–1494.

Xu, Z. G., Ding, L. L., Du, X. L., Xu, C. S., & Zhuang, H. Y. (2023b). Generalized response displacement methods for seismic analysis of underground structures with complex cross section. *Earthquake Engineering and Engineering Vibration, 22*(4), 979–993.

Xu, M., Cui, C., Zhao, J., Xu, C., Zhang, P., & Su, J. (2024). Fuzzy seismic fragility analysis of underground structures considering multiple failure criteria. *Tunnelling and Underground Space Technology, 145*, 105614.

Xu, M., Cui, C., Liu, H., Li, J., Zhao, J., & Xu, C. (2025a). Non-parametric probabilistic seismic capacity model for the stochastic interaction system of soil-subway station structures. *Underground Space, 24*, 79–103.

Xu, M., Cui, C., Zhao, J., Xu, C., & Meng, K. (2025b). A novel approach to seismic fragility evaluation of underground structures considering hybrid epistemic uncertainties of both seismic demand and capacity. *Tunnelling and Underground Space Technology, 156*, 106278.

Yu, J. K., Wang, R. X., Zhang, J. M., & Wang, R. (2025). High-performance seismic response analysis for mega-scale integrated underground-aboveground structure system in saturated sand. *Fundamental Research*. In press.

Zhang, J. M., & Wang, R. (2024). Large post-liquefaction deformation of sand: Mechanisms and modeling considering water absorption in shearing and seismic wave conditions. *Underground Space, 18*, 3–64.

Zhao, M., Ding, Q. P., Cao, S. T., Li, Z. S., & Du, X. L. (2024). Large-scale seismic soil–structure interaction analysis via efficient finite element modeling and multi-GPU parallel explicit algorithm. *Computer Aided Civil and Infrastructure Engineering, 39*(12), 1886–1908.

Zhu, T., Hu, J., Zhang, Z., Zhang, J. M., & Wang, R. (2021a). Centrifuge shaking table tests on precast underground structure–aboveground structure system in liquefiable ground. *Journal of Geotechnical and Geoenvironmental Engineering, 147*(8), 04021055.

Zhu, T., Wang, R., & Zhang, J. M. (2021b). Evaluation of various seismic response analysis methods for underground structures in saturated sand. *Tunnelling and Underground Space Technology, 110*, 103803.

Zhu, T., Wang, R., & Zhang, J. M. (2021c). Effect of nearby ground structures on the seismic response of underground structures in saturated sand. *Soil Dynamics and Earthquake Engineering, 146*, 106756.